DOI: 10.13009/EUCASS2023-487
Aerospace Europe Conference 2023 – 10TH EUCASS – 9TH CEAS

Radio Communication Blackout Mitigation: Ray Tracing Analysis and Signal Characterization Including Experimental Validation for Non-magnetized Plasmas

J. S. Laur[⋆]†*, D. Luis*[⋎,⋇]*, A. Viladegut*[⋎]*, V. F. Giangaspero*[⋄]*, A. Lani*[⋄]*, J. L. Gonzalez Rios*[⋆]*,*
J. Querol[⋆], J. Vasquez Peralvo[⋆], J. C. Merlano Duncan[⋆], A. Hein[⋆] and J. Thoemel[⋆]
[⋆]*University of Luxembourg*
6 Rue Richard Coudenhove-Kalergi, 1359 Kirchberg Luxembourg
[⋎]*Von Karman Institute for Fluid Dynamics*
Chaussee de Waterloo 72, 1640 Rhode-Saint-Genese, Belgium
[⋇]*Universitat Polictecnica de Catalunya*
UPC Campus Nord, C/Jordi Girona 1-3, 08034 Barcelona, Spain
[⋄]*KU Leuven*
Celestijnenlaan 200B, Leuven, 3001, Belgium
johannes.laur@uni.lu · j.thoemel@uni.lu
†Corresponding author

Abstract

Atmospheric entries are a crucial part of space missions involving the possible loss of goods, data, and life in case of malfunctions. The cut-off of communication, also known as a radio communication blackout, is caused by the plasma surrounding the hypersonic (entry) vehicle in case the critical electron number density exceeds the radio frequency of the antenna. Mitigating radio communication blackouts during hypersonic flights and atmospheric entries is in the interest of the European Union's Horizon 2020 project MEESST (Magnetohydrodynamic Enhanced Entry Systems for Space Transportation), alongside heat flux reduction and radiation mitigation using a high-temperature superconducting magnet. The BlackOut RAy Tracer (BORAT), a ray tracing method to predict the signal propagation in the plasma domain surrounding a hypersonic (entry) vehicle, was further developed. As characterizing the electromagnetic signal emerging from a radiation source like an antenna is essential for a better understanding of the nature behind the cut-off of communication, this feature was added to the latest version of BORAT. Two methods are analyzed and compared. One method called the Ray Density Refinement method, subsequently refines the ray density at the receiving antenna positions, which is used to increase the accuracy by marginally increasing the computational resources. The second method is called the Ray method. After propagating through the plasma area, the latter distributes the ray information discretely on the ray aperture.

The method is validated using on-ground plasma wind tunnel experiments conducted at the von Karman Institute for Fluid Dynamics (VKI). The experimental setup contains one transmitting and one receiving antenna connected via a Vector Network Analyzer (VNA) measuring the scattering parameters, the magnitude and phase of the ratio of the received and transmitted signal. A new model is implemented to account for the realistic transmitting and receiving radiation patterns, respectively, for better agreement between the numerical fluid simulations in combination with the added ray tracing and signal characterization analysis and the experiment. The results from the numerical tools show a good agreement with the experimental measurements conducted at VKI. Possible errors like plasma fluctuations, numerical errors, and signal losses are considered.

1. Introduction

Atmospheric entries are a challenging part of a space mission. Flights at hypersonic speeds are generally challenging due to a plasma enveloping the vehicle.v A shock in front of the entry spacecraft is formed by the atmospheric gas flowing by the vehicle. The gas is heated due to the shock and friction resulting in the dissociation and ionization of molecules and atoms. This ionized gas flow, or plasma, disables or partially disrupts communication, telemetry, and data for global positioning to ground stations or relay satellites.[1–3] This principle is described in Fig. (1). The

DOI: 10.13009/EUCASS2023-487

cut-off of communication, also known as a radio communication blackout, is mainly caused by the free electrons in the plasma, which are refracting, reflecting, or totally attenuating the electromagnetic wave transmitting or receiving from an onboard antenna. The blackout occurs for a non-magnetized plasma with negligible collisions when the plasma

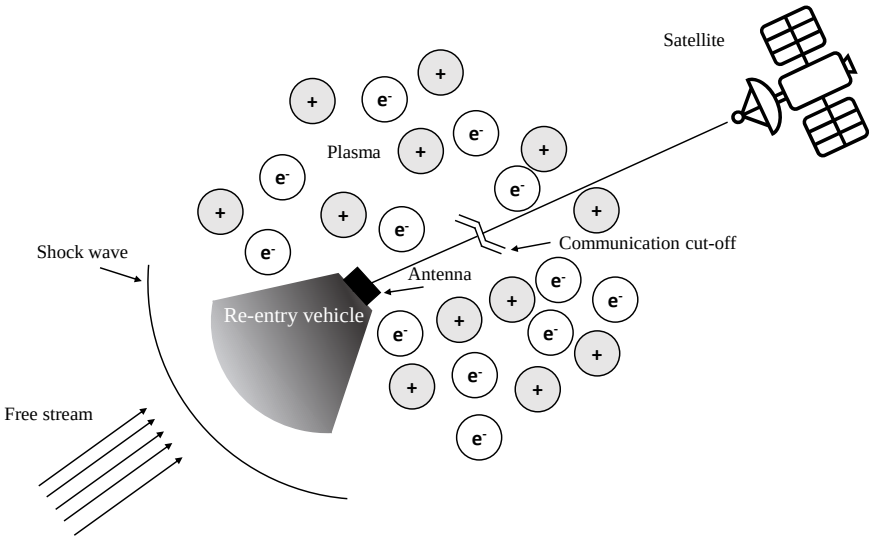

Figure 1: Schematic of the reason for cut-off of communication.[4]

frequency exceeds the radio frequency as described Eq. (1):

$$f_{radio} \leq f_{plasma} = \frac{1}{2\pi}\sqrt{\frac{e^2 N_{e_{crit}}}{\epsilon_0 m_e}}, \tag{1}$$

with f_{radio} as the radio frequency, f_{plasma} as the plasma frequency, e as the electron charge, m_e as the electron mass, and $N_{e_{crit}}$ as the critical electron number density. The signal attenuation per unit length over the electron number density for various frequencies including the corresponding critical electron number densities for the L-, S-, X-, and Ka-band are plotted in Fig. (2).[5,6] Blackout conditions are reached when the plasma frequency is equal to or greater than the radio frequency. The critical electron number density for L-band is for example $3.5 \cdot 10^{18}\mathrm{m}^{-3}$, and $1.3 \cdot 10^{19}\mathrm{m}^{-3}$ for Ka-band. The electron number densities also depend on the trajectory and the shape of the vehicle. Usual electron number densities during atmospheric entries are between $10^{15}\mathrm{m}^{-3}$ and $10^{19}\mathrm{m}^{-3}$ according to the literature.[7] Techniques for mitigating radio communication blackouts were intensively investigated and summarized in literature.[1] A short overview is given in the following list.

1. The aerodynamic shaping method makes use of the advantage that some electromagnetic waves with a wavelength much longer than the plasma sheath thickness might be able to propagate through the plasma sheath. A sharp body produces a thin less ionized plasma sheath.

2. The Liquid Quenchant Injection method aims to reduce the electron number density by "quenching" the plasma by injecting liquids.

3. The Solid Quenchant Mitigation method is similar to the Liquid Quenchant Injection method but using solid material to quench the plasma.

4. Guolong He[3] mentions also the Resonant Transmission method, and the Inflatable Aeroshell method for radio communication blackout mitigation.

5. The Magnetic Window method uses the advantage of changing the dispersion relation, or refractive index, of the plasma. Recent developments in high temperature superconducting magnets brought focus back on the Magnetic Window method.

DOI: 10.13009/EUCASS2023-487

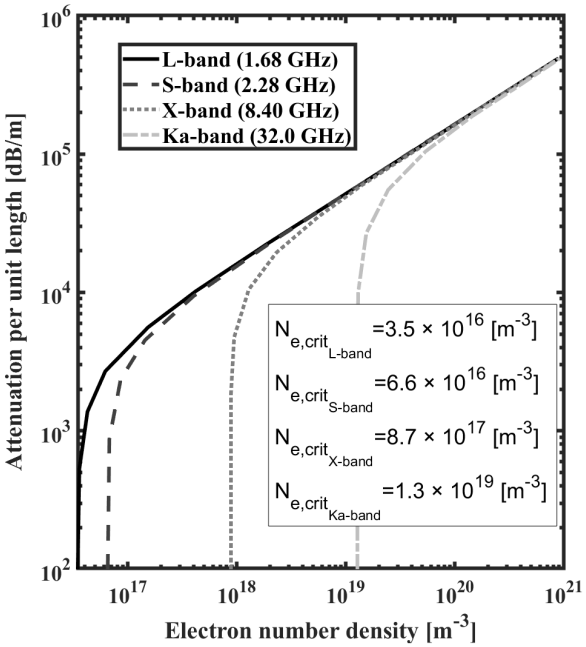

Figure 2: Attenuation per unit length over electron number density for various frequencies with their critical electron number densities.[5,6]

This work is part of the EU Horizon 2020 Magnetohydrodynamic Enhanced Entry System for Space Transportation (MEESST) project. MEESST aims to reduce the heat flux, and the radiation on the vehicle, and mitigate radio communication blackout by applying a sufficiently strong magnetic field using a cryo-cooled high-temperature superconductive magnet.[8] A schematic of the magnetic window effect is shown in Fig. (3). The volume around the magnet contains fewer free electrons. The reduction of the electron number density leads to a different dispersion relation, or refractive index, of the plasma in this area enabling the radio waves to propagate through the plasma.

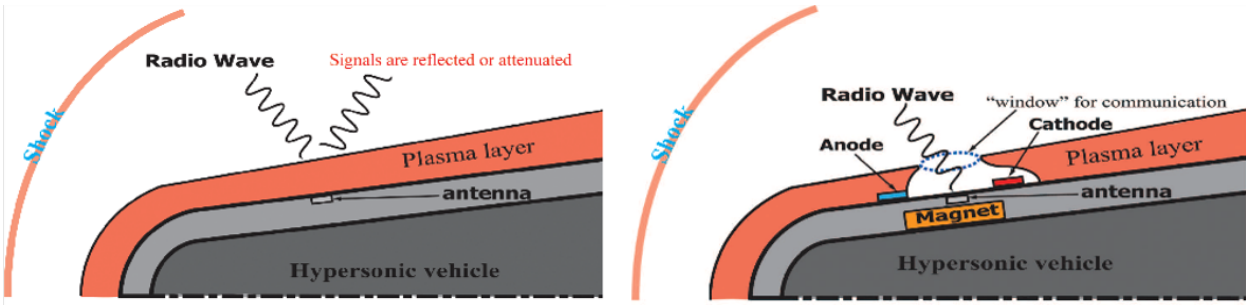

(a) (b)

Figure 3: Illustration of RF interaction with a plasma sheath above the critical plasma frequency (a) without and (b) with an applied magnetic field and the created magnetic window.[6]

This article focuses only on the communication aspect of MEESST. The radio communication blackout is analyzed by using a ray tracing technique. Ray tracing is commonly used in the field of optics and wireless communication systems to analyze the propagation of electromagnetic waves. Ray tracing is also commonly used in fusion plasma. A summary of existing ray tracing models for fusion plasma can be found here.[9] It can be used to characterize a signal by tracing the path of the wave as it travels through various mediums or reflects off different surfaces. Overall, the use of ray tracing can provide valuable insights into how a signal propagates through a given environment, allowing for more effective design and optimization of communication systems.[10,11] New ray tracing techniques for atmospheric entries were recently published, which analyzed blunt cones and inhomogeneous plasma slabs.[12,13] Vecchi et al. published a ray tracing model and analyzed the Atmospheric Re-entry Demonstrator (ARD)[14] and the Intermediate eXperimental Vehicle (IXV).[15] However, none of those publications fully analyze the signal propagation in combination with a

DOI: 10.13009/EUCASS2023-487

signal characterization for arbitrary inhomogeneous plasma with arbitrary incident waves for any possible fluid composition. The latest publication by A. Scarabosio et al. related to atmospheric entries and ray tracing also includes an Electromagnetic (EM) wave analysis. However, in their work, only the transmitting side of an antenna on the vehicle is considered.[16] Within MEESST the BlackOut RAy Tracer (BORAT), originally developed by Jan Thoemel (https://github.com/JanThoemel/borat), is used. In this work, we present the progress of raytracing algorithms based on the Eikonal equations and Snell's law and include the physics of wave propagation. The latest version of BORAT can perform a 2D ray tracing analysis for non-magnetized plasma in combination with the signal characterization. The scattering parameter is calculated by applying the Friis transmission equation on the rays reaching the receiving antenna considering various effects like the free space loss, polarization changes, interference, and transmission mismatches. BORAT is extensively tested and validated with on-ground experiments performed by our MEESST project partner at the Von Karman Institute for Fluid Dynamics (VKI).

In section 2 the relevant plasma properties and BORAT and its development stages are introduced. The wave properties and antenna theory are elaborated as well. In section 3 the results of the validation are presented. Section 4 is concluding the work.

2. Methodology

First, the BORAT development stages are explained in this section, followed by the rationale for the latest version of BORAT (version 5.0). Afterward, the optical properties of plasmas are described, and the ray tracing solvers are introduced. Lastly, the methodology for the signal characterization is explained.

2.1 BORAT Development Stages

In BORAT 1.0 the Snell's law solver is applied to calculate the ray propagation path according to the geometrical optics in the refractive index field in the numerical flow domain. BORAT 2.0 was developed by Vincent F. Giangaspero (KU Leuven) with the novel Eikonal Solver. The latter, based on wave optics, is faster than the Snell's law solver and at least as accurate. Computation time was essential for extending the ray tracing algorithm to 3D, leading to developing BORAT 3.0. In this version, the third dimension is added by Vincent F. Giangaspero.[17] BORAT 4.0 was developed to analyze the effect of an applied magnetic field and is therefore capable of calculating the ray propagation path in magnetized plasma using the Snell's law solver. The signal characterization is added in BORAT 5.0 to investigate the effects of the plasma on a radio signal without the effect of an applied magnetic field. An overview of the BORAT versions is shown in Fig. (4).

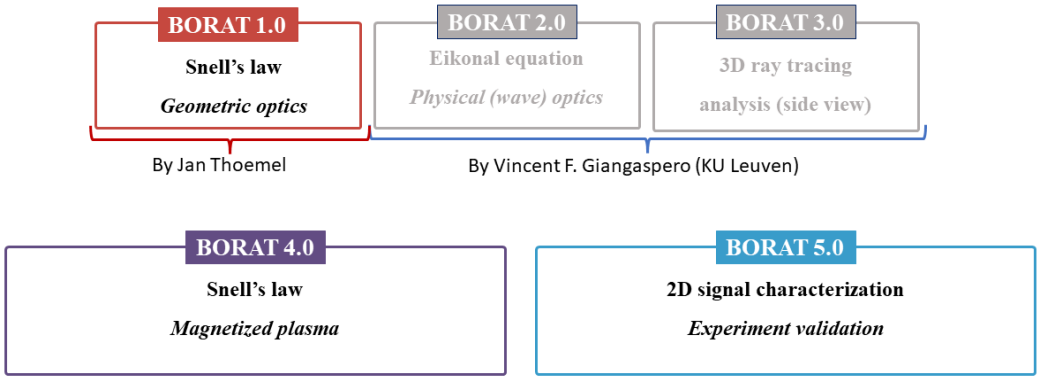

Figure 4: BORAT development stages.

2.2 Rationale for the BlackOut RAy-Tracer with Signal Characterization - BORAT 5.0

The rationale of BORAT 5.0 is shown in Fig. (5). A numerical analysis of the radio communication blackout using BORAT requires a Computational Fluid Dynamics (CFD) simulation as input. Decoupling the ray tracing analysis

DOI: 10.13009/EUCASS2023-487

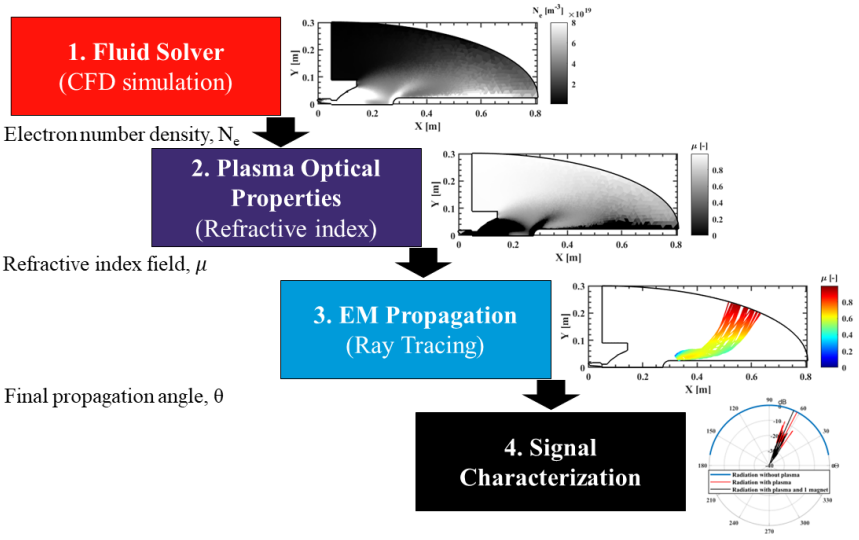

Figure 5: Rationale for BORAT with Signal Characterization for Magnetized Plasma.

from the fluid computation is valid since the time scales for multi-species hypersonic flows are in the range of milliseconds and the time scale of radio waves is in nanoseconds.[18] This enables the usage of any CFD software by adding the required I/O capabilities in BORAT. The required fluid properties inside the flow domain, e.g., gas composition, temperature models, and magnetic field information, are acquired. In the next step, the electron number densities in the flow domain are calculated from the obtained fluid properties.

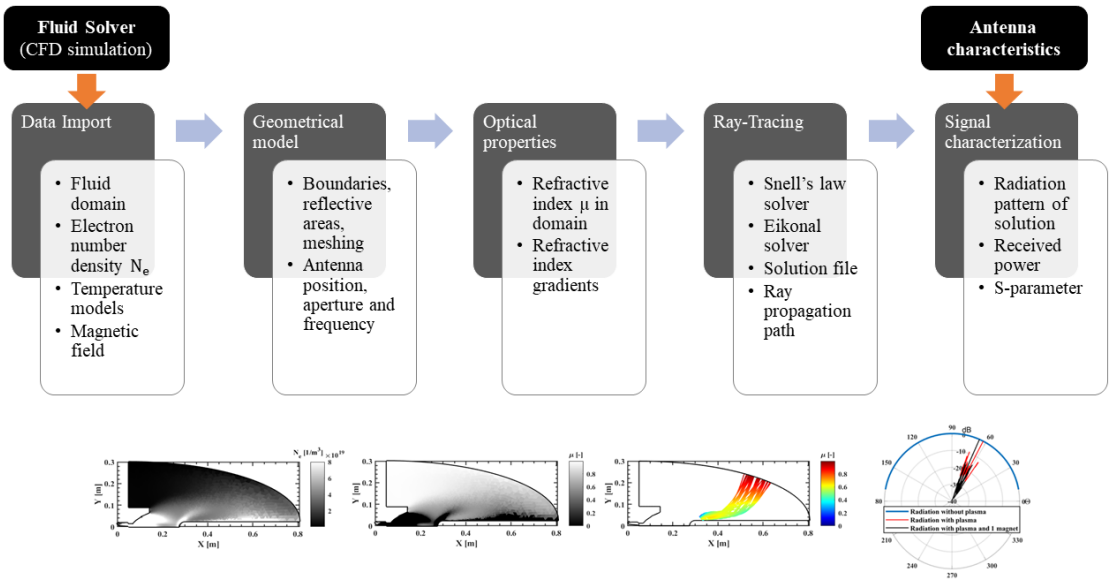

Figure 6: Workflow of BORAT with Signal Characterization for non-magnetized Plasma.

Afterwards, the plasma optical properties are calculated using the Appleton-Hartree equation (see section 2.3). The Snell's law solver or the Eikonal solver is then used to predict the ray propagation depending on the antenna aperture, antenna position, the refractive index field.

The ray tracing solution together with the information of the transmitting antenna characteristics is required as input to characterize the radio signal. The power received by the receiving antenna and the scattering parameter are calculated and possible errors are estimated. A detailed workflow is described in Fig. (6).

DOI: 10.13009/EUCASS2023-487

2.3 Plasma Optical Properties

The cold plasma approximation is valid for atmospheric entries or hypersonic flow plasmas since we are only concerned by radio signals traveling close to the vacuum speed of light in plasmas with a thermal electron velocity much smaller than the speed of light.[19] The full Appleton-Hartree equation (2) describes the refractive index for magnetized cold plasmas including collisions. This form of the Appleton-Hartree equation is suitable to show the relation between the wave vector and the magnetic field by including the angle Θ between the wave vector and the magnetic field:[20]

$$n^2 = (\mu - \chi i)^2 = 1 - \frac{X}{1 - Zi - \frac{Y^2 sin^2(\Theta)}{2\,(1 - X - Zi)} \pm \sqrt{\frac{Y^4 sin^4(\Theta)}{4\,(1 - X - Zi)^2} + Y^2 cos^2(\Theta)}}. \tag{2}$$

with:

$$\begin{aligned} X &= e^2 N_e / \left(\epsilon_0 m \omega^2\right) \\ Y &= eB / (m\omega) \\ Z &= \nu / \omega \\ \omega &= 2\pi f \end{aligned} \tag{3}$$

where e denotes the electron charge, N_e the electron number density, ϵ_0 the vacuum permittivity, m_e the electron mass, ν the electron-heavy particle collision frequency, f for the communication system transmission frequency and B is the magnetic field. The ± sign represents the polarization of the electromagnetic wave with "+" for the right-hand polarized wave and "-" for the left-hand polarized wave.[21] It is worth mentioning that the wave vector is independent of the refractive index in the cold plasma approximation.[19] The refractive index might change while the electromagnetic wave is propagating through the magnetized plasma because of the link between the wave vector and the magnetic field through the angle Θ. Additionally, the refractive index values are not limited between 0 and 1 if compared to the collision-free non-magnetized solution of the Appleton-Hartree equation and can become complex.[22]

2.3.1 Non-magnetized plasma - Neglecting collisions

In case collisions are negligible and no magnetic fields are applied the equation to calculate the refractive index simplifies as follows:

$$n = \mu = \sqrt{1 - X} = \sqrt{1 - \left(\frac{f_p}{f}\right)^2}, \tag{4}$$

The refractive index becomes a function of the plasma frequency f_p and the radio frequency f in Hz. The refractive index for non-magnetized plasma neglecting collisions is a real number between 0 and 1. The value for the refractive index decreases for a given antenna frequency f if the electron density N_e is increasing, i.e., while the EM wave is propagating into regions with higher electron density concentration the refractive index μ becomes smaller.

2.4 BORAT Ray Tracing Solver

2.4.1 Snell's Law Solver

The Snell's Law is the governing equation of geometrical optics and is the most simplified model for EM wave propagation in a medium. The Snell's law ray tracing integration technique is an iterative marching technique that assumes discrete, straight wave propagation over small distances. The rays are emitted at the antenna location and the direction of the ray is determined using the laws of geometrical optics. The deviation of a ray's path from a straight line is computed by using Snell's law:

$$\mu_1 \sin\alpha_1 = \mu_2 \sin\alpha_2 \tag{5}$$

This algorithm is a marching-in-space method, and the signal is modeled as a ray that advances for a chosen finite distance, also known as the marching step.[23] A schematic of the procedure is shown in Fig. (7). A chosen step size in the domain represents a region of constant refractive index, which is called an iso-surface. Snell's Law is then applied at the boundaries of the iso-surfaces. The marching technique starts by advancing one step size from P_1 to $P_{1.5}$. The refractive index is determined at $P_{1.5}$ and the algorithm then go back to P_{temp} by advancing backwards at half the step size. The radius of the iso-surface and its associated normal is found. Snell's Law is then applied between P_1 and

DOI: 10.13009/EUCASS2023-487

$P_{1.5}$ to find α_2. The algorithm then advances to P_2 by advancing half the value of the step size from P_{temp} at an angle α_2. The process is repeated until a border of the domain is reached or the attenuation of the signal reaches a threshold. Significantly, the step size for the raytracer needs to be chosen small enough to accurately resolve the gradients in the refractive index within the flow field, which is ensured with a step size independence study.

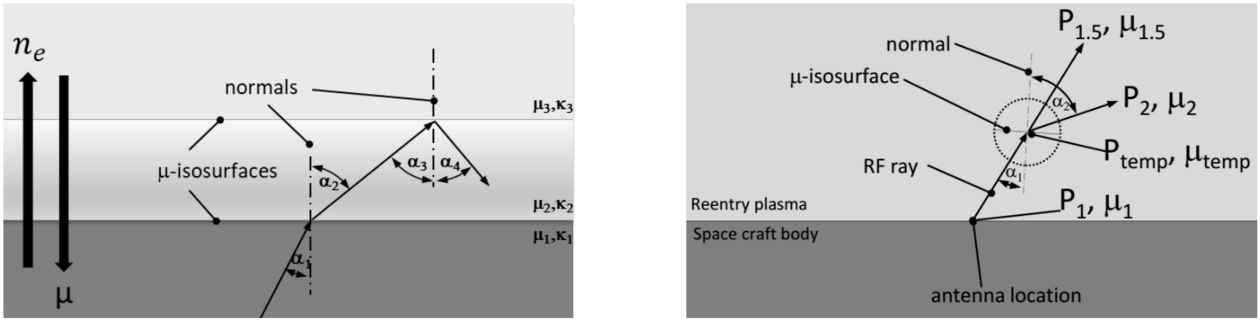

Figure 7: Snell's law ray tracing algorithm: Snell's Law (left) and Marching technique (right).

In a typical reentry application case, the rays emerging from an antenna at the vehicle's surface move from a relatively cold region with lower electron densities (or a higher index of refraction) to hotter regions with higher levels of electron concentration (or a lower refractive index). This is analogous to light transitioning from water into air or from a medium that is optically dense to a medium that is less dense. As the rays penetrate into higher levels of electron concentration, μ falls lower and lower. If the electron density is sufficiently large to reduce μ to zero, then a wave will be reflected as described by equation (5) and shown in Fig. (7). Thus, Snell's law will have no solution when the critical angle is exceeded and consequently the law of reflection is applied.

2.4.2 Eikonal Solver

The Eikonal equation is the direct link between geometrical optics and EM waves theory, and it is the theoretical starting point of any physical and advanced raytracing method. The Eikonal equation can be derived as an approximate solution of Maxwell's equations in the high-frequency limit.[17,24] The Eikonal approximation is valid as long as medium properties vary slowly over a length-scale of the order of the signal wavelength.[17,24] In a hypersonic entry plasma, this assumption can be considered valid in the whole wake region, while the front shock region, characterized by steep gradients, is generally not involved in EM propagation. At large frequencies, electric and magnetic fields may be expressed as:

$$\begin{aligned} E(r) &\simeq E_0 e^{-\imath k_0 S(r)} \\ H(r) &\simeq H_0 e^{-\imath k_0 S(r)}, \end{aligned} \tag{6}$$

where $S(r)$ is the normalized Eikonal phase function, defining the wave-front surface, and k_0 is the wave number. Inserting the high frequency fields into Maxwell's equations leads to the Eikonal equation:

$$|\nabla S| = \mu, \tag{7}$$

that defines the relation between the direction of propagation of an EM wave and the refractive index μ of the medium.

A more convenient, but mathematically equivalent, form of the Eikonal equation may be obtained by rewriting the equation in characteristic form. The characteristic solution of the Eikonal equation defines the rays' trajectories. This may be achieved by introducing the normalized local wave vector $\xi = \nabla S$, that defines the propagation direction of the EM wave, and the position vector $x_i = (x_1, x_2)$. Using the arc-length s along the ray, one arrives at the following system of ordinary differential equations:

$$\begin{aligned} \frac{\partial x_i}{\partial s} &= \frac{\xi_i}{\mu}, \\ \frac{\partial \xi_i}{\partial s} &= \frac{\partial \mu}{\partial x_i}. \end{aligned} \tag{8}$$

The system (8), along with prescribed initial conditions in terms of position and angle of the emitted ray, allows to predict ray trajectories and states that the curvature of rays at each point is proportional to the gradient of the

DOI: 10.13009/EUCASS2023-487

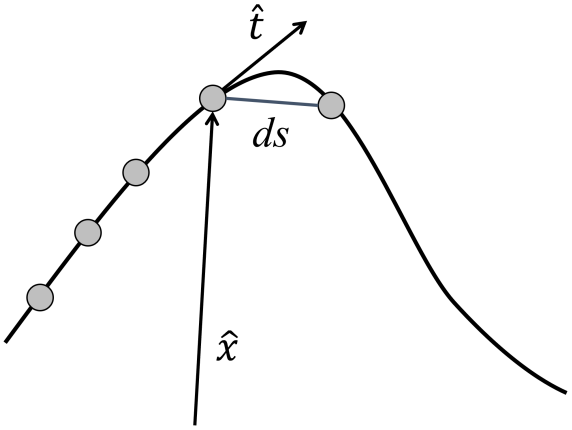

Figure 8: Ray trajectory for Eikonal algorithm.

refractive index, as illustrated in Fig. (8). The validity of the characteristic solution of the Eikonal equation, namely the ray trajectories, falls in layers of plasma in which the value of the refractive index μ vanishes. These conditions are generally referred as cut-off conditions, and they are treated as localized reflection conditions. However, these conditions are rarely encountered, since in re-entry plasma problems high-density electron layers with steep variations are generally located in the front part of the vehicle, not designed for communication propagation.

From a theoretical point of view, from the Eikonal equation is possible to retrieve the Snell's law equation. In a uniform refractive index field medium, the gradient of the refractive index is equal to zero. Integrating the Eikonal equation leads to a linear variation in space of the ray trajectory:

$$\nabla n = 0 \rightarrow n = const \rightarrow \frac{\partial^2 x_i}{\partial s^2} = 0 \rightarrow \bar{x} = \bar{a}s + \bar{b} \tag{9}$$

Thus, the Snell's law can be considered as the local solution of the Eikonal equation at the interface between two mediums at different refractive index, in which a straight ray deviates depending on the refractive index discontinuity at the interface. The Eikonal formulation presents three main advantages. First, second-order continuity in the refractive index of the Eikonal formulation allows us to increase the ray tracing solution accuracy with respect to the first-order raytracing Snell's law algorithm. Second, the Ordinary Differential Equations (ODE) system resulting from the Eikonal equation (8) is solved using a Runge-Kutta method (RK4) with adaptive integration step refinement. This leads to a performance increase up to 100x times with respect to the previous marching-in-space method. Last, one of the main advantages of the Eikonal system of equation is the decoupled form of the space variables, allowing algorithmic simplicity that led to a straightforward development of a 3D version of the solver.

Refractive index gradients, which are needed for Eikonal equation integration, are reconstructed from the plasma field with a first order approximation:

$$\mu\,(x, y, z) = \frac{\partial \mu}{\partial x} x + \frac{\partial \mu}{\partial y} y + \mu_0 \tag{10}$$

The refractive index $\mu(x, y, z)$ is assumed to be a piece-wise planar function over the computational domain. For each computational domain mesh element, the reconstructed gradient is computed by solving the following system of equations:

$$\begin{bmatrix} x_1 & y_1 & 1 \\ x_2 & y_2 & 1 \\ x_3 & y_3 & 1 \end{bmatrix} \begin{bmatrix} \frac{\partial \mu}{\partial x} \\ \frac{\partial \mu}{\partial y} \\ \mu\,(x, y) \end{bmatrix} = \begin{bmatrix} \mu(x_1, y_1) \\ \mu(x_2, y_2) \\ \mu(x_3, y_3) \end{bmatrix} \tag{11}$$

where:

$$\nabla \mu|_{_T} = \begin{bmatrix} \frac{\partial \mu}{\partial x} & \frac{\partial \mu}{\partial y} \end{bmatrix} \tag{12}$$

DOI: 10.13009/EUCASS2023-487

The partial derivative at each node is the weighted sum of each of the partial derivatives of the triangles associated with that node. The weightings $\omega_i = A_i/A_{tot}$ are the areas of each triangle divided by the total area of all triangles associated with that node.

$$\nabla\mu|_n = \sum_{i=1}^{k} \omega_i \nabla\mu|_{T_i} \tag{13}$$

A more detailed description of the Eikonal solver can be found here.[17]

2.5 Signal Characterization

The novel signal characterization model to estimate the possible received power at an antenna and to analyze the effect of plasma is described in the following.

The input for the signal characterization is, besides the ray tracing solution, the directivity patterns or the (complex) electric field patterns of the receiving and the transmitting antenna, respectively. The antenna input power, of the transmitting antenna and the antenna mismatch is required as well. The antenna gain can either be calculated from the radiation pattern or be provided as additional input data.

2.5.1 Calculation of the Received Power at a Receiving Antenna

The received power P_r is calculated by applying the Friis transmission equation on each ray reaching the receiving antenna:[25]

$$P_r = e_{cdt} e_{cdr} (1 - |\Gamma_t|^2)(1 - |\Gamma_r|^2) \left(\frac{\lambda}{4\pi R}\right)^2 D_t(\Theta_t, \Phi_t) D_r(\Theta_r, \Phi_r) |\hat{\rho_t} \cdot \hat{\rho_r}|^2 P_t, \tag{14}$$

with

$$|\hat{\rho_t} \cdot \hat{\rho_r}|^2 = \cos(\psi_p)^2 \tag{15}$$

where D_t and D_r are the directivities of the transmitting and receiving antenna, respectively, e_{cdt} and e_{cdr} are the combined dielectric and conductive antenna efficiencies, $(1 - |\Gamma_t|^2)$ and $(1 - |\Gamma_r|^2)$ are the efficiencies due to reflection mismatch, $|\hat{\rho_t} \cdot \hat{\rho_r}|^2$ is the power loss factor due to polarization mismatch of the incoming wave and the receiving antenna with the angle ψ_p between the polarization vectors (see Fig. (9)). P_t and P_r are the transmitted and received power without antenna losses, the distance between the antennas or the wave path is R, and the wavelength of the electromagnetic wave is λ. The angle ψ_p in rad between the polarization vectors is obtained from the Faraday rotation

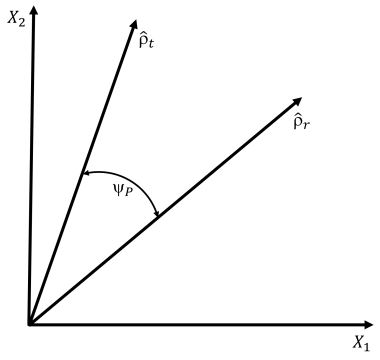

Figure 9: Schematic of the angle ψ_p between the polarization vectors of the incoming wave and the receiving antenna.[25]

along the wave path:[26]

$$\psi_p = 2.36 \cdot 10^4 \frac{B \cdot N_T}{f^2}, \tag{16}$$

with B as the magnetic field, f the electromagnetic wave frequency, and the total electron count (TEC) N_T. The equation for TEC is given below:

$$N_T = \int_S n_e(s) ds, \tag{17}$$

with the electron number density n_e along the propagation path s.

DOI: 10.13009/EUCASS2023-487

Possible interference between rays reaching the receiving antenna aperture is considered by converting the ray propagation path length differences into a phase shift and calculating the interference loss factor (IFL) by applying the following equation:

$$ILF = cos\left(\frac{\Delta L}{\lambda} \cdot 2\pi\right), \tag{18}$$

with ΔL as the ray propagation length difference between the receiving rays, and the wavelength λ. Each ray is defined over an angle $\Delta\Theta$ according to the angular ray density. This angle defines a ray tube. A ray tube is an area associated with the ray at a path length on which the energy of the ray is acting. This ray tube is increasing for increasing path lengths and is calculated for each ray reaching the receiving antenna. Depending on the position of the ray hitting the antenna aperture its contributing effective area on the antenna aperture $A_{ray_{eff}}$ can be smaller than its actual ray tube area A_{ray}. Their ratio, as described in Eq. (19), describes the area loss factor (ALF):

$$ALF = \frac{A_{ray_{eff}}}{A_{ray}}. \tag{19}$$

The equation for the receiving power P_r for each ray including ILF and ALF reads as follows:

$$P_r = e_{cdt}e_{cdr}(1 - |\Gamma_t|^2)(1 - |\Gamma_r|^2)\left(\frac{\lambda}{4\pi R}\right)^2 D_t(\Theta_t, \Phi_t)D_r(\Theta_r, \Phi_r)\cos(\psi_p)^2 cos\left(\frac{\Delta L}{\lambda} \cdot 2\pi\right)\left(\frac{A_{ray_{eff}}}{A_{ray}}\right)P_t. \tag{20}$$

2.5.2 Effective Antenna Area and Total Received Power

The effective antenna area $A_{ant_{eff}}$ of the receiving antenna on which the transmitted radio signal is captured is calculated as follows:[28]

$$A_{ant_{eff}} = \frac{\lambda^2 G}{4\pi}, \tag{21}$$

with λ as the wavelength of the radio signal, and G as the receiving antenna gain.

Friis transmission equation describes the total power received in a specific direction. The received power P_r using Friis transmission equation is calculated for each ray reaching the receiving antenna. Hence, the mean received power over all rays needs to be calculated as follows:

$$P_{r_{mean}} = \frac{1}{N}\sum_{1}^{N} P_r, \tag{22}$$

with N as the number of rays reaching the receiving antenna. Additional losses $P_{loss_{additional}}$ [dB] in experiments, e.g cable losses, adapter losses, or windows, need to be considered, which leads to the following equation for the total received power $P_{r_{total}}$ [dB]:

$$P_{r_{total}} = P_{r_{mean}} - P_{loss_{additional}}. \tag{23}$$

2.5.3 Scattering Parameters

The antenna measurements are often performed using a Vector Network Analyzer (VNA), which measures the amplitude and phase of the wave quantities.[29] The magnitude of the complex S-parameters describes the amplitude ratio of the received to the transmitted sinusoidal signal generated by the VNA and the phase of the complex S-parameter corresponds to the phase difference between the incoming and outgoing waves at each port of the VNA. In the definition of power waves the waves traveling away from a port of a n-port VNA are $\mathbf{a} = (a_1, a_2, ..., a_n)$ and the waves traveling towards a port are $\mathbf{b} = (b_1, b_2, ..., b_n)$ and are described as follows:[30]

$$\begin{aligned} a_i &= \sqrt{2P_{a_i}}, \text{and} \\ b_i &= \sqrt{2P_{b_i}}. \end{aligned} \tag{24}$$

Since we are only interested in the amount of power that is delivered to one or several receiving antennas from one transmitting antenna we ignore the self-reflection at the ports and are only concerned about the S-parameters S_{b_2,a_1} to S_{b_n,a_1}. Hence, these S-parameters describe the ratio of the received to the transmitted power.

$$\begin{aligned} S_{b_2,a_1} &= \sqrt{\frac{P_{b_2}}{P_{a_1}}}, \\ &..., \\ S_{b_n,a_1} &= \sqrt{\frac{P_{b_n}}{P_{a_1}}} \end{aligned} \tag{25}$$

DOI: 10.13009/EUCASS2023-487

Hereby, P_{a_1} stands for the transmitted power P_t, and P_{b_i} with $i = 2-n$ stands for the received power P_r at each receiving antenna.

2.5.4 Signal Characterization in BORAT

The signal characterization in BORAT is implemented by two different methods, the Ray Density Refinement method, and the Ray method. The signal characterization was implemented as add on to the ray tracing analysis. After the raytracing solution is produced using Snell's law solver or the Eikonal solver either of the two methods can be applied. Ray Density Refinement method:

1. The rays closely reaching the antennas are identified and their original starting angle is obtained.
2. A second ray tracing analysis is started using the identified min. and max. initial radiation angles of each receiving antenna.
3. The rays hitting the receiving antenna aperture are identified and their receiving power is calculated according to Eq. (20).
4. The power of each ray is added, and the losses of the equipment are subtracted using Eq. (23).
5. The S-parameters are calculated according to Eq. (25).

Ray method:

1. The ray density is artificially increased by adding discrete points along the initial ray aperture angle (angular distance between two adjacent rays) with the same information of the ray propagation as the corresponding ray.
2. The points hitting the receiving antenna aperture are identified and their receiving power is calculated according to Eq. (20).
3. The power of each ray is added, and the losses of the equipment are subtracted using Eq. (23).
4. The S-parameters are calculated according to Eq. (25).

3. BORAT Verification and Validation

3.1 BORAT Validation with On-Ground Experiments at VKI

The on-ground validation experiments are performed in the Plasmatron plasma wind tunnel facility at VKI.[8] The static chamber pressure of the selected operating conditions is 15 mbar with an input power of 100 kW. Since the BORAT analysis is performed in 2D and wall reflections are not considered the operating conditions are limited to cases in which the rays are not totally reflected by the plasma stream. A broader analysis will be performed in 3D including the effect of an applied magnetic field in future work. The experimental setup consists of one receiving antenna and one transmitting antenna on opposite sides of the vacuum chamber with an axial distance of 300 mm from the torch exit as sketched in Fig. (10).[26] The antennas are conical horn antennas with linear polarization (MI-wave 262A-15/0.250), each connected to a mode transition (MI-wave 284-0.250) and a waveguide to coax adapter (MI-wave 411A). The transmitting side is connected via a 3 m, and the receiving side via a 3.5 microwave cable from Huber-Suhner (SUCOFLEX 102). The S-parameters are measured using a VNA (Rhode and Schwarz ZNB 40), with DC blocks (MI-wave 8141A) installed in each port. Details of each component can be found in Table (1).[26] The antenna radiation patterns are experimentally measured in the anechoic chamber at the Universitat Politecnica de Catalunya (UPC).[27] The measurements are taken at frequencies between 33 and 40 GHz. The measured electric fields radiated by the antenna at 34, 37, and 40 GHz are

Table 1: Details about the equipment used for the experiments.[26]

Instruments	Antenna	Mode transition	Adaptor	Cable	DC block	VNA
Connectors	custom flange	custom flange	custom flange - 2.92 mm (f)	2.92 mm (m-f)	2.92 mm (m-f)	2.92 mm (m)
Operating frequency [GHZ]	33 - 38.5	33 - 38.5	26.5 - 40	up to 46	0.01 - 40	0.01 - 40
Link budget	15 dBi	0 dB	- 0 .4 dB	-2.62 dB/m	- 0.75 dB	0 dBm

converted into directivity patterns as can be seen in Fig. (10). Those radiation patterns are rotated into the transmitting antenna direction. The corresponding pattern for the receiving antenna is rotated by 180°.

DOI: 10.13009/EUCASS2023-487

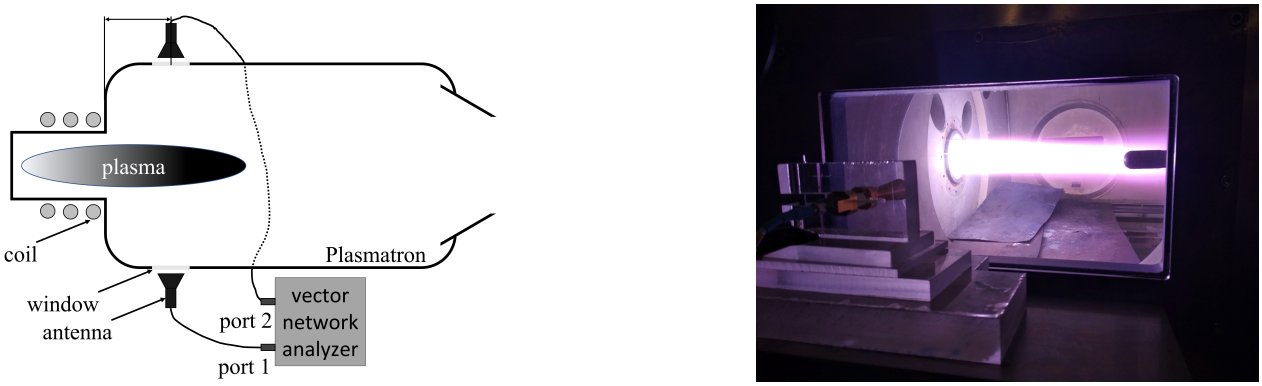

Figure 10: Schematic of the antenna positions with respect to the CFD domain (a) and a photograph with one of the antennas during a test in the Plasmatron (b).[26]

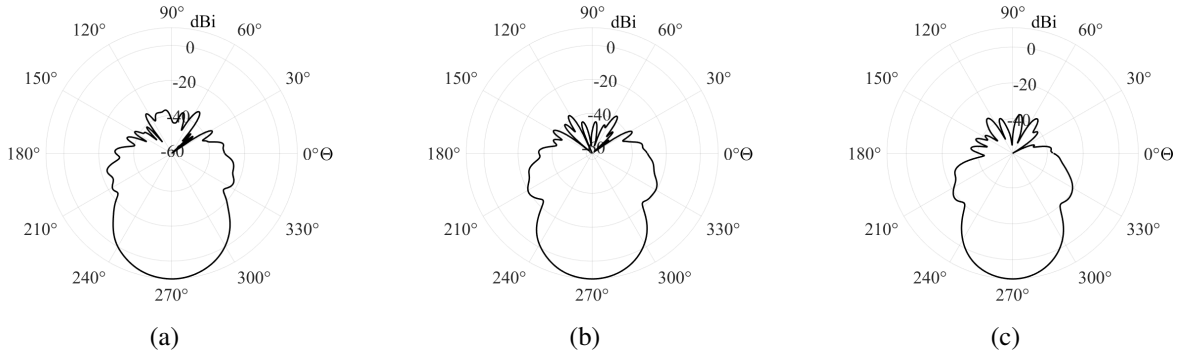

Figure 11: Antenna directivity pattern for frequencies of (a) 34 GHz, (b) 37 GHz, and (c) 40 GHz.[26]

Non-Plasma Validation Case The ray tracing solution for the non-plasma case is shown in Fig. (12 (a)). The straight lines starting from the transmitting antenna at the top of the domain (x = 0.786 m, y = 0.399 m) are computed until they reach the domain boundary. The vacuum chamber diameter of the Plasmatron is 1.4 m. The computational flow domain is limited in diameter to reduce computational resources, The ray density for all simulations is one ray per degree. The flow domain is increased around the torch area compared to the schematic in Fig. (10 (a)) including a cylindrical probe at y = ±0.025 m and x > 0.931 m. Showing the non-plasma ray tracing solution shall give a better understanding of how the signal propagation is changing when an input power of 100 kW is applied 3.1 over various frequencies. Since no plasma is present, the radiation patterns are not affected, similar to the ray propagation.

The error estimation of the experiment takes the standard deviation of the measurements into account, as well as the manufacturing errors of 0.5 dB of the antenna gain, and an error of ±10% of the equipment. The error estimation of the BORAT simulations takes a power fluctuation of ±5%, an interpolation error of ±3%, and an ray tube error of ±10% into account. The antenna efficiency is assumed to be 100%. Both signal characterization methods show a good agreement with the experimental values as can be seen in Fig. (12). At 34 GHz the ray density refinement is in the upper error area while the Ray method is at the lower error area. The discrepancies between the two methods are decreasing for higher frequencies and moving towards the upper error area of the experiments. An antenna efficiency of less than 100% would improve the agreement between the Ray Density Refinement method and the experiments but deteriorate the S-parameter of the Ray method.

Plasma Validation Case The ray tracing solutions for the plasma case at 15 mbar static chamber pressure and 100 kW input power is shown in Fig. (13). The effect of the plasma on the ray propagation is decreasing if the frequency is increasing as expected.

The corresponding radiation (directivity) patterns after propagating through the plasma are shown in Fig. (14). The ray tracing solution is limited to a 36° aperture to avoid reflections on the probe, which was not present in the experiment. This results in displaying a small section of the total radiation pattern. The radiation intensity is increasing for all frequencies compared to the initial radiation pattern in Fig. (11) because of the plasma. At 40 GHz the peak is exactly in receiving antenna direction.

DOI: 10.13009/EUCASS2023-487

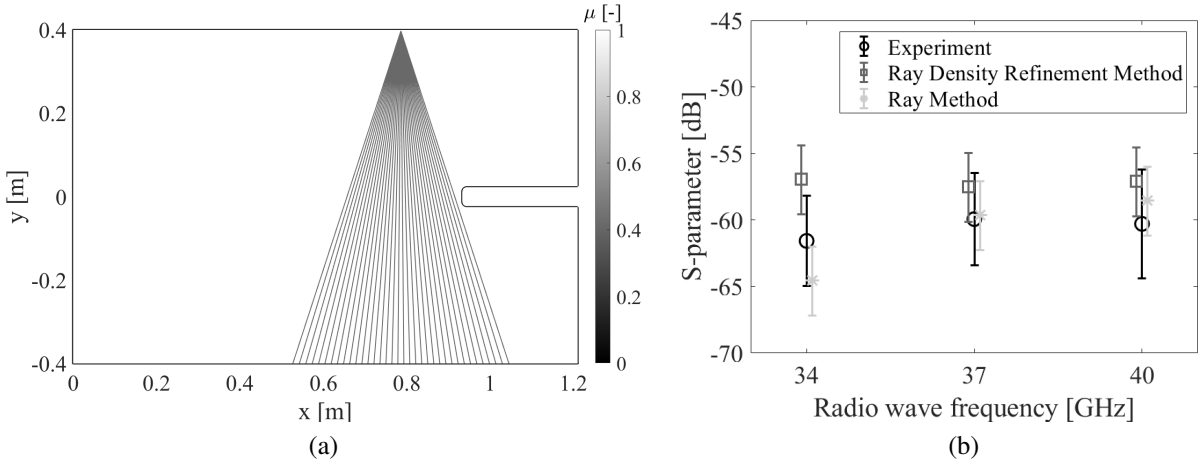

Figure 12: Ray tracing solution of the MEESST side-to-side non-plasma case (a), and the resulting S-parameter over various radio frequencies (b).

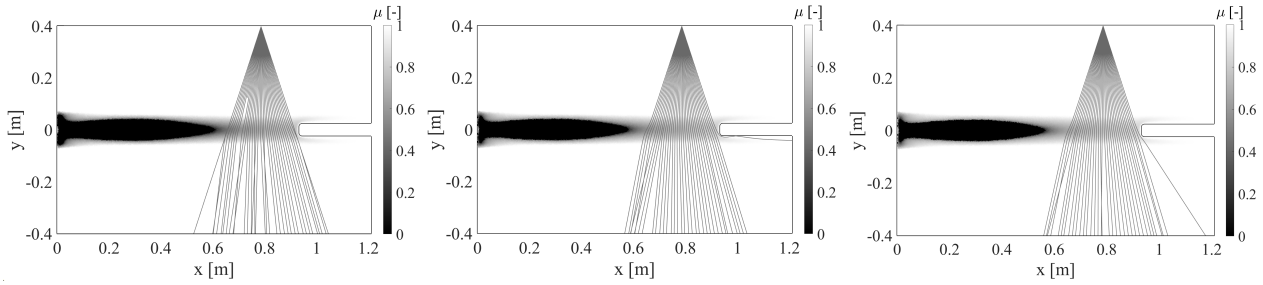

Figure 13: Ray tracing solutions for the MEESST side-to-side plasma case at 15 mbar static chamber pressure and 100 kW power for (a) 34 GHz, (b) 37 GHz, and (c) 40 GHz.

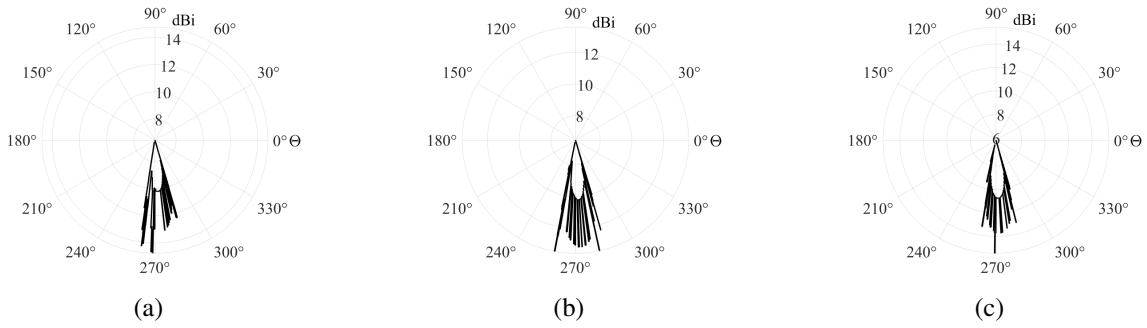

Figure 14: Directivity pattern for the MEESST side-to-side plasma case at 15 mbar static chamber pressure and 100 kW power for (a) 34 GHz, (b) 37 GHz, and (c) 40 GHz after propagation through the plasma.

The S-parameter analysis is shown in Fig. (15). First, the Faraday rotation caused by Earth's magnetic field, the transmission line mismatch, and the free space loss are considered. Since we neglect heavy particle collisions in the refractive index calculation, no plasma attenuation is present. Fig. (15 (a)) clearly shows a divergence of the numerical results compared to the experimental results for increasing frequencies. Second, the effect of an additional magnetic field induced by the current in the plasma coil is analyzed in Fig. (15 (b)). The total Faraday rotation is calculated using the magnetic field distribution in the line of sight of the antennas. The additional magnetic field has no significant effect on the signal characterization. Third, the interference with the rays reaching the receiving antennas is analyzed in Fig. (15 (c)). This shows a good agreement between the Ray Density Refinement method and the experiments. The Ray method is clearly not valid for this case. It seems that the ray density is too small. The behavior of the Ray method agrees with the before described peak in the radiation pattern for the case of a frequency of 40 GHz (see 14).

DOI: 10.13009/EUCASS2023-487

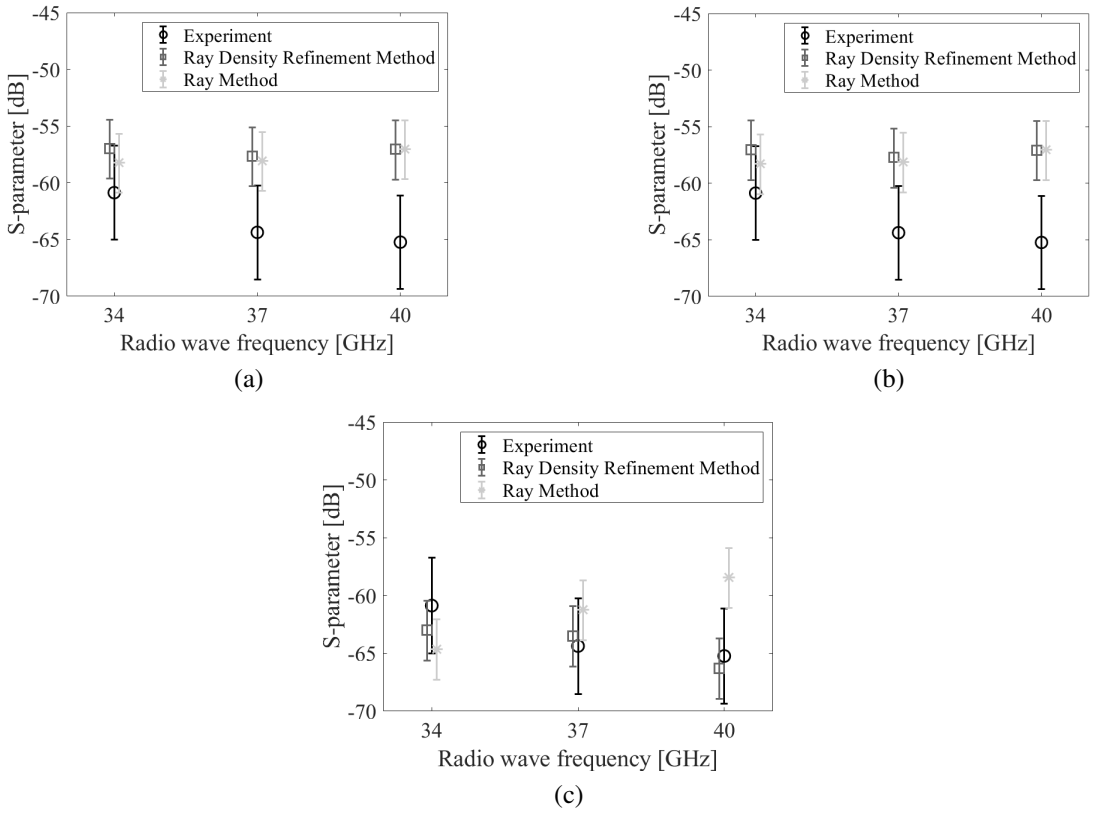

Figure 15: S-parameter over various radio frequencies for the MEESST side-to-side plasma case at 15 mbar static chamber pressure and 100 kW power for (a) the Faraday rotation caused by Earth's magnetic field, (b) the additional Faraday rotation due to the induced current of the coil, and (c) including interference for case (a).

4. Conclusion

The novel signal characterization approach, especially the Ray Density Refinement method is valid. The results of all test cases are within the error margins. The faster Ray method requires a smaller initial ray density to improve the accuracy of the results, which reduces its computational performance. This would increase the overall computation time of BORAT. Future analysis will be performed only using the Ray Density Refinement method, since for this method the accuracy can be easily improved with a higher ray density on a small radiation angle in the second ray tracing step. The effect of the induced magnetic field is negligible, at least for experiments at low power. The interference shows a significant contribution to the accuracy of the solution.

5. Acknowledgments

This work and the whole MEESST project were supported by the European Innovation Council (EIC) Pathfinder programme of the European Commission's Horizon 2020 scheme [grant no. 899298].

Diana Luis' research is funded by a doctoral fellowship (2021.04930.BD) granted by Fundação para a Ciência e Tecnologia (FCT Portugal).

The authors would especially like to acknowledge the help of Prof. Sebastián Blanch from UPC for performing and processing the antenna pattern measurements conducted at the UPC anechoic chamber.

References

[1] Eric D. Gillman, John E. Foster, and Isaiah Blankson. Review of leading approaches for mitigating hypersonic vehicle communications blackout and a method of ceramic particulate injection via cathode spot arcs for blackout mitigation. 2010.

DOI: 10.13009/EUCASS2023-487

[2] Michael Keidar, Minkwan Kim, and Iain D. Boyd. Electromagnetic reduction of plasma density during atmospheric reentry and hypersonic flights. *Journal of Spacecraft and Rockets*, 45(3):445–453, may 2008.

[3] Guolong He, Yafeng Zhan, and Ning Ge. ADAPTIVE TRANSMISSION METHOD FOR ALLEVIATING THE RADIO BLACKOUT PROBLEM. *Progress In Electromagnetics Research*, 152:127–136, 2015.

[4] Yusuke Takahashi, Reo Nakasato, and Nobuyuki Oshima. Analysis of radio frequency blackout for a blunt-body capsule in atmospheric reentry missions. *Aerospace*, 3(1):2, jan 2016.

[5] Georg Herdrich. Raumfahrtrelevante plasmen und deren anwendungsbezogene klassifizierung, 2012.

[6] K. Minkwan, M. Keidar, and I. D. Boyd. Analysis of an electromagnetic mitigation scheme for reentry telemetry through plasma. *Journal of Spacecraft and Rockets*, 45(6):1223–1229, 2008.

[7] Minkwan Kim and Ali GÃ¼lhan. Plasma manipulation using a mhd-based device for a communication blackout in hypersonic flights. In *Proceedings of 5th International Conference on Recent Advances in Space Technologies - RAST2011*, pages 412–417, 2011.

[8] Andrea Lani, Vatsalya Sharma, Vincent F. Giangaspero, Stefaan Poedts, Alan Viladegut, Olivier Chazot, Jasmine Giacomelli, Johannes Oswald, Alexander Behnke, Adam S. Pagan, Georg Herdrich, Minkwan Kim, Neil D. Sandham, Nathan L. Donaldson, Jan Thoemel, Juan C.M. Duncan, Johannes S. Laur, Sonja I. Schlachter, Rainer Gehring, Matthieu Dalban-Canassy, Julien Tanchon, Veit Große, Pénélope Leyland, Angelo Casagrande, Manuel La Rosa Betancourt, Marcus Collier-Wright, and Elias BÃ¶gel. A magnetohydrodynamic enhanced entry system for space transportation: Meesst. *Journal of Space Safety Engineering*, 10(1):27–34, 2023.

[9] Hua-sheng Xie, Banerjee Debabrata, Yu-kun Bai, Han-yue Zhao, and Jing-chun Li. Boray: An axisymmetric ray tracing code supports both closed and open field lines plasmas, 05 2021.

[10] J.-P. Rossi and A. J. Levy. A ray model for decimetric radiowave propagation in an urban area. *Radio Science*, 27(06):971–979, 1992.

[11] Aliye Ozge Kaya, Larry J. Greenstein, and Wade Trappe. Characterizing indoor wireless channels via ray tracing combined with stochastic modeling. *IEEE Transactions on Wireless Communications*, 8(8):4165–4175, 2009.

[12] Linjing Guo, Lixin Guo, and Liping Gan. Investigation of effects of plasma sheath on antenna radiation based on ray tracing method. *AIP Advances*, 11(8), 08 2021. 085116.

[13] Junyang Zhou and Yiping Han. Analysis of plasma sheath propagation attenuation based on ray tracing. *Contributions to Plasma Physics*, 62(1):e202100071, 2022.

[14] C Vecchi, M Sabbadini, R Maggiora, and A Siciliano. Modelling of antenna radiation pattern of a re-entry vehicle in presence of plasma. In *IEEE Antennas and Propagation Society Symposium, 2004.*, volume 1, pages 181–184. IEEE, 2004.

[15] A. Scarabosio, J. L. Araque Quijano, J. Tobon, M. Righero, G. Giordanengo, D. DAmbrosio, L. Walpot, and G. Vecchi. Radiation and scattering of em waves in large plasmas around objects in hypersonic flight, 2021.

[16] Andrea Scarabosio, Javier Leonardo Araque Quijano, Jorge Tobon, Marco Righero, Giorgio Giordanengo, D. D'Ambrosio, L. Walpot, and Giuseppe Vecchi. Radiation and scattering of EM waves in large plasmas around objects in hypersonic flight. *IEEE Transactions on Antennas and Propagation*, 70(6):4738–4751, jun 2022.

[17] Vincent F. Giangaspero, Vatsalya Sharma, Johannes Laur, Jan Thoemel, Alessandro Munaf, Andrea Lani, and Stefaan Poedts. 3d ray tracing solver for communication blackout analysis in atmospheric entry missions. *Computer Physics Communications*, 286:108663, 2023.

[18] Madhusudhan Kundrapu, John Loverich, Kris Beckwith, Peter Stoltz, Michael Keidar, Alexey Shashurin, and Taisen Zhuang. Modeling and simulation of weakly ionized plasmas using nautilus. 01 2013.

[19] I. H. Hutchinson. *Principles of Plasma Diagnostics*. Cambridge University Press, 2 edition, 2002.

[20] Hema Singh, Simy Antony, and Rakesh Mohan Jha. *Plasma-based Radar Cross Section Reduction*. Springer Singapore, 2016.

DOI: 10.13009/EUCASS2023-487

[21] Yunxian Tian, Weizhong Yan, Xiaoliang Gu, Xiaolin Jin, Jianqing Li, and Bin Li. Effects of magnetized plasma on the propagation properties of obliquely incident THz waves. *AIP Advances*, 7(12):125325, dec 2017.

[22] K. Davies. *Ionospheric radio propagation*, volume 80. US Department of Commerce, National Bureau of Standards, 1965.

[23] S. Ramjatan, A. Lani, S. Boccelli, B. Van Hove, Ö Karatekin, T. Magin, and J. Thoemel. Blackout analysis of mars entry missions. *Journal of Fluid Mechanics*, 904, 2020.

[24] Yury A Kravtsov and Yuri Ilich Orlov. *Geometrical optics of inhomogeneous media*, volume 38. Springer, 1990.

[25] Constantine A. Balanis. *Antenna theory : : analysis and design /.* Wiley, Hoboken, New Jersey, fourth edition. edition, 2016 - 2016.

[26] A. Viladegut A. Lani A. Camps O. Chazot D. Luis, V. F. Giangaspero. Effect of electron number densities on the radio signal propagation in an inductively coupled plasma facility. 2023 (not published yet).

[27] Anechoic chamber UPC. https://www.tsc.upc.edu/en/facilities/anechoic-chamber. Accessed: 2023-07-02.

[28] Klaus W. Kark. *Antennen und Strahlungsfelder*. Vieweg+Teubner, 2010.

[29] M. Hiebel. *Fundamentals of Vector Network Analysis*. Rohde & Schwarz, 2007.

[30] F. Caspers. Rf engineering basic concepts: S-parameters. 2012.